Article

Regional Algorithm for Estimating High Coccolithophore Concentration in the Northeastern Part of the Black Sea

Svetlana Vazyulya [1], Dmitriy Deryagin [1,2], Dmitry Glukhovets [1,2,*], Vladimir Silkin [1] and Larisa Pautova [1]

[1] Shirshov Institute of Oceanology of the Russian Academy of Sciences, 117997 Moscow, Russia; vasyulya.sv@ocean.ru (S.V.); dmitriy.deryagin@phystech.edu (D.D.); vsilkin@mail.ru (V.S.); larisapautova@ocean.ru (L.P.)
[2] Moscow Institute of Physics and Technology, 141700 Dolgoprudny, Russia
* Correspondence: glukhovets@ocean.ru; Tel.: +7-(499)124-75-83

Abstract: A modified regional algorithm to quantify the coccolithophore concentration in the northeastern part of the Black Sea under conditions of intense bloom is presented. To modify the algorithm, the data of in situ measurements of coccolithophore *Emiliania huxleyi* abundance performed in June 2017 and 2022 (when the maximum values were 9×10^6 and 13×10^6 Cells L^{-1}, respectively), as well as the data from hydro-optical and satellite measurements, were used. In addition, the ratio between the number of detached coccoliths and coccolithophore cells was taken into account. Based on the expanded array of in situ data, the optimal values of the regional algorithm parameters were obtained. The modified algorithm makes it possible to obtain more accurate results in areas of high coccolithophore concentrations and takes into account the contribution of coccoliths. To test the sensitivity of the algorithm to variations in bio-optical characteristics, model calculations were performed using Hydrolight software. The updated algorithm is significantly less sensitive to variations in chlorophyll concentration and CDOM absorption coefficient than its previous version.

Keywords: coccolithophore bloom; Hydrolight; ocean color; quantitative phytoplankton analysis; remote sensing reflectance

1. Introduction

Phytoplankton in the world ocean play an important role in the regulation of the planet's climate. They contain almost half of all carbon assimilated [1,2]. The ocean is the main depositor of absorbed atmospheric carbon; it has 50 times more carbon than the atmosphere [3–5]. The flow of carbon dioxide at the ocean–atmosphere boundary, its biological assimilation into the ocean water, and the further transfer of carbon in organic form from the upper layers to the deep ocean and to the ocean floor is carried out through a process called the 'carbon pump' [6,7]. Due to this, carbon pump global carbon export occurs, and it is currently estimated at between 5 and 15×10^{15} g of carbon per year [8,9]. At the ocean–atmosphere interface, the transport of CO_2 molecules takes place. Its speed and direction depend on the difference in the partial pressures of carbon dioxide in the atmosphere and in the ocean surface layer.

In water, phytoplankton convert dissolved carbon into organic form through photosynthetic reactions, and this process is called the 'organic pump', while some researchers suggest the term 'soft tissue pump' [10]. Diatoms are mainly responsible for the operation of the organic pump in the ocean [11]. The concentration of chlorophyll is an indicator reflecting the functioning of the organic pump [12].

However, in the ocean, evolution has proposed another biological way of fixing dissolved carbon. Calcite is a mineral formed by calcium carbonate ($CaCO_3$). It is also formed in the ocean in addition to organic carbon. This type of carbon assimilation process is called the 'carbonate pump'; the main contributors to its work are coccolithophores, which have one important property of forming a calcite cell shell [13–15]. This shell consists of separate

plates—coccoliths. The release of a CO_2 molecule, as a result of the formation of a single calcite molecule, is important for the functioning of the carbonate pump. In other words, if the organic pump reduces the partial pressure of carbon dioxide in water, the carbonate pump, in contrast, increases it. Therefore, during the coccolithophore bloom (CB), the concentration of carbon dioxide in the water increases and, as a result, there is a significant decrease in its flow into the water or even its release into the atmosphere [16–18]. Therefore, the ratio of diatoms and coccolithophores is a fundamental indicator characterizing the state of the carbonate system [19].

Emiliania huxleyi is the main phytoplankton species that determines the functioning of the carbonate pump in the ocean. This species is widespread throughout the Northern and Southern Hemispheres, but its blooms are recorded mainly in high latitudes [20–24]. In the Black Sea, the intensive growth in coccolithophore abundance was noted in the 1950s [25]. In the beginning of this century, their role in the phytoplankton structure increased, as was noted in field observations [26–28]. Long-term observations of the phytoplankton structure in the northeastern part of the Black Sea have established that in the end of May and beginning of June, an intensive growth of *Emiliania huxleyi* is observed almost annually, and the abundance of this species exceeds 10^6 Cells L^{-1} [28].

The method of field observations does not allow creation of a unified picture of coccolithophore bloom distributions. Such capabilities are provided by ocean remote sensing, which allows blooms to be studied in a wide range of spatial and temporal scales. Only remote sensing methods give an opportunity to obtain the data necessary for the creation of carbon export global models from the upper layers to the deep ocean [9]. Coccolithophores differ from other phytoplankton species in terms of strong low-selective light scattering, which makes it possible to observe bloom according to satellite ocean color scanner data [15,29–33]. Satellite data are used to observe the CB in the Black Sea, starting with the SeaWiFS ocean color data [34]. The results of observations show that during late spring and early summer, extensive bloom areas are observed, covering most of the sea [29,35–40].

Previously, a regional algorithm for the northeastern part of the Black Sea based on bio-optical measurements from 2004–2008 was developed to evaluate the coccolithophore concentration [29]. Using this algorithm, monthly average maps and diagrams for the period 1998–2018 were drawn, and were presented in the Atlas of Bio-optical Characteristics of the Ocean Optics Laboratory at the Shirshov Institute of Oceanology of the Russian Academy of Sciences (SIO RAS) [41]. However, the coccolithophore concentrations obtained in the expeditions, using the results of which this algorithm was created, did not exceed 2.5×10^6 Cells L^{-1} in most cases. They are significantly lower than the values that can be observed during the period of intense blooms. For example, according to the regional algorithm, the monthly average concentration of coccolithophores in June 2017 exceeded 6×10^6 Cells L^{-1} [41]. Such a significant difference in the range of values used for the algorithm development with the results of its application requires verification and appropriate modification of the regional algorithm.

Specifically, the purpose of this work is the development of a new algorithm for high coccolithophore and coccolith concentrations using the latest data from in situ and simultaneous satellite measurements.

2. Materials and Methods

For our purpose, the data from in situ and simultaneous satellite measurements in the northeastern part of the Black Sea near Gelendzhik (44.56°N, 38.08°E) in June 2017 and 2022, obtained during the period of intense coccolithophore blooms, were used. In situ measurements included both a complex of hydrooptical works and laboratory measurements of coccolithophore plated cell and detached coccolith abundance. The median coccolithophore concentration in the upper mixed layer according to direct measurements in those years was 7 and 5.4×10^6 Cells L^{-1}. Along with the expansion of the field measurements dataset, model data obtained using Hydrolight 6.0 software [42] were used to modify the algorithm.

2.1. Study Area and Bio-Optical Measurements

The complex optical measurements were performed in June 2017 and 2022 on the small research vessel *Ashamba* on the transect from the Blue Bay (near Gelendzhik) to the center of the sea (Figure 1a) with simultaneous ocean color satellite observations accompanied by hydrological and biogeochemical studies. Favorable weather conditions provided good-quality remote sensing data.
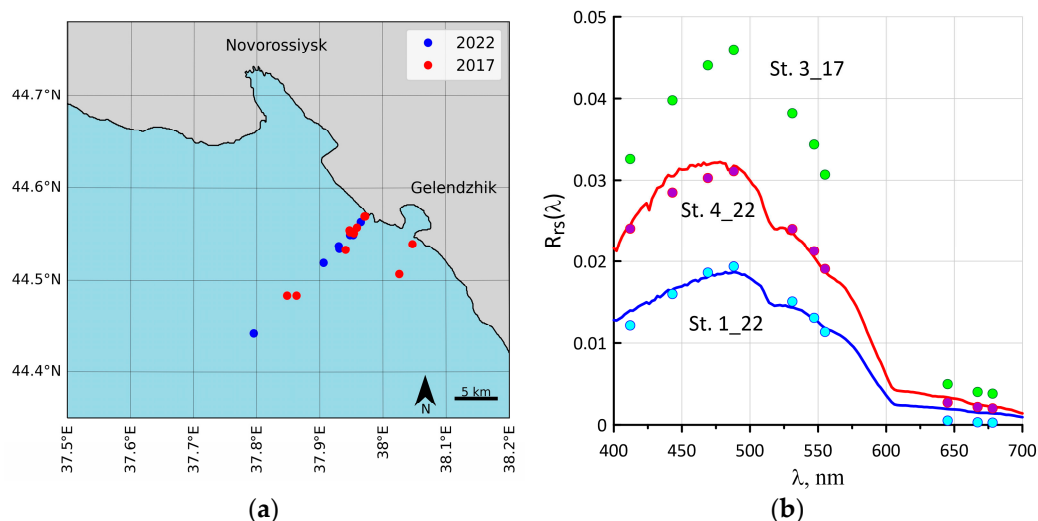

Figure 1. (**a**) Map of stations. (**b**) Examples of $R_{rs}(\lambda)$ spectra measured using the floating spectroradiometer PRO-1 (solid lines) and calculated from MODIS data (circles).

For a number of stations in 2022, the spectra of the remote sensing reflectance $R_{rs}(\lambda)$ were obtained using the floating spectroradiometer PRO-1 [43]. The floating spectroradiometer was developed at SIO RAS and allows the measurement of spectral values of the surface downwelling irradiance $E_d(\lambda,0^+)$ and the upwelling radiance below the sea surface $L(\lambda,0^-)$. From the obtained values the water, radiance reflectance $\rho(\lambda)$ is calculated, which then is converted to $R_{rs}(\lambda)$, using the following formula [44]:

$$R_{rs}(\lambda) = 0.165\, \rho(\lambda)/[1 - 0.497\, \rho(\lambda)]. \tag{1}$$

PRO-1 works in the spectral range of 390–700 nm with a spectral resolution of 2.5 nm; its accuracy is about 5%.

Figure 1b shows examples of $R_{rs}(\lambda)$ values measured with the help of the floating spectroradiometer PRO-1 in comparison with satellite data for two stations from June 11, 2022. The observed difference in spectra is explained well by the distinction in the intensity of CB at these stations; according to direct measurements, the coccolithophore concentration at station 1_22 was 4.8×10^6 Cells L^{-1}, and at station 4_22 it was 9.3×10^6 Cells L^{-1}.

A submerged transmissometer PUM-200 developed at SIO RAS [45] was used to measure vertical profiles of the beam attenuation coefficient at a 530 nm wavelength $c(530)$. These profiles are quite valuable, as the $c(530)$ profile depicts the vertical distribution of the coccolithophore layer. PUM-200 measurements made it possible to determine the thickness of the coccolithophore layer Z_{coc}.

2.2. Sampling

At the stations (Figure 1a), water samples were taken from different depths for laboratory determination of the spectral absorption coefficient of colored dissolved organic matter (CDOM) $a_g(\lambda)$, the concentration of chlorophyll *a* (*Chl*), and the species composition of phytoplankton. Water samples were taken using 5-L Niskin bathometers mounted on a Rosette sampler.

An integrated cavity absorption meter (ICAM) was used to measure the absorption spectra of seawater, filtrates, and suspended particles [46,47]. The difference between the values of the filtrate and pure water absorption coefficients allowed the estimation of the CDOM absorption coefficient $a_g(\lambda)$. The biogeochemical parameters also included the concentrations of chlorophyll *a* and pheophytin *a* measured using a fluorometric method [48,49].

Samples for determining the species composition of phytoplankton were fixed using neutralized formaldehyde (final concentration 0.8–1.0%). Sample settling was the main method of cell concentration. The identification of the species and counting of the cells were carried out using a light microscope at 16×10 and 16×40 magnifications. Identification was based on the described morphology [50,51] (http://www.algaebase.org, accessed on 18 April 2022, and http://www.marinespecies.org, accessed on 18 April 2022). The nano- and microplankton cells were counted using 0.05 mL Nageotte and 1 mL Naumann counting chambers [27]. The small flagellates (2–4, 4–6, and 6–8 μm fractions) and coccoliths were counted using a Finuchs–Rosenthal counting chamber. A method based on the geometric shape of cells was used to calculate biomass [52,53]. The number of coccolithophores equal to 1×10^6 Cells L^{-1} was taken as the bloom threshold concentration [24].

In our study, we used the results of determining the concentration of coccolithophore cells N_{cc} and separated coccoliths N_{cl}. Light scattering occurs both on coccolithophore cells and on detached coccoliths. According to the work presented in [54], the values of the specific backscattering coefficients for a coccolith are, on average, 50 times lower than for a coccolithophore cell, that is, the contribution to the backscattering of 50 coccoliths and one cell is approximately the same. Therefore, according to direct measurements, the value of N_{cc_cl} was calculated as

$$N_{cc\_cl} = N_{cc} + N_{cl}/50, \qquad (2)$$

while the average values for the two upper depths were used (the first one was 0 m, the second was 5–11 m).

2.3. Satellite Data

We used the Level 2 data of the satellite spectroradiometers Moderate-Resolution Imaging Spectroradiometer (MODIS)-Aqua and MODIS-Terra, Visible Infrared Imaging Radiometer Suite (VIIRS)-SNPP and VIIRS-JPSS, available through the NASA website [55]. Satellite data processing was performed using the SMCS 1.9 software package developed at the SIO Ocean Optics Laboratory [56].

The spectra of the remote sensing reflectance $R_{rs}(\lambda)$ in the pixel closest to the station were selected for the stations. Two satellite datasets were selected: in the first, shipboard and satellite measurements were performed on the same day, and in the second, satellite data were added on the previous and subsequent days. Thus, in the first dataset, the time difference between shipboard and satellite measurements did not exceed 8 h, and in the second 32 h. Examples of the comparison of satellite (from the first dataset) and in situ $R_{rs}(\lambda)$ for two stations in 2022 are shown in Figure 1b. It also shows an example of the MODIS spectrum for station 3_17 in 2017 with laboratory estimates of $N_{cc\_cl} = 11.6 \times 10^6$ Cells L^{-1}.

2.4. Regional Algorithm 2014

Based on field measurements of coccolithophore concentration N_{coc} performed in 2004–2008, a regional algorithm for estimating N_{coc} from satellite data in the Black Sea was created [29]. According to this algorithm, the backscattering coefficient is determined by three components:

$$b_{bp} = b_{bp\_bg} + b_{bp\_riv} + b_{bp\_coc}, \qquad (3)$$

where b_{bp_bg} is its background value, b_{bp_riv} is the backscattering coefficient due to terrigenous suspended matter brought by river runoff, and b_{bp_coc} is responsible for the presence of coccolithophores and coccoliths in seawater. The value of b_{bp_bg} was selected as the lowest monthly means of $b_{bp} = 0.0025$ m^{-1}, derived from satellite data over the period

2003–2010. To account for the contribution of terrigenous suspension, the following formula was used:

$$b_{\text{bp\_riv}} = K_{\text{riv}} (a_{\text{g}} - a_{\text{g\_bg}}), \tag{4}$$

where a_g and $a_{\text{g\_bg}}$ are the absorption coefficients of CDOM at the wavelength 440 nm. The first is determined in the algorithm [29] as a result of solving the inverse problem of obtaining two unknown model parameters (a_{g} and N_{coc}) from the R_{rs} spectra for two wavelengths. The second is determined similarly to $b_{\text{bp\_bg}}$ based on the minimum values of satellite a_{g} estimates for 2003–2010, and is equal to 0.047 m^{-1}. We used the following expression for coccolithophore suspension:

$$b_{\text{bp\_coc}} = K_{\text{coc}} N_{\text{coc}}. \tag{5}$$

The following values of K_{coc} and K_{riv} were obtained: $K_{\text{coc}} = 2.74 \times 10^{-3}$ and $K_{\text{riv}} = 0.157$ [29].

To find two parameters of the model, the use of two spectral MODIS bands is proposed: 488 and 555 nm. In the case of VIIRS, we used close bands: 489 and 556 nm for JPSS, and 486 and 551 nm for SNPP. For model R_{rs} spectra obtained using Hydrolight, we used bands 488 and 551 nm.

The error estimation results for the in situ and satellite R_{rs} spectra for the obtained algorithm turned out to be close (standard errors 1.15 and 0.99 $\times$ 10^6 Cells L^{-1}). The differences are due to the different dataset used for these estimates. Moreover, in both cases, the average concentration of N_{coc} according to the results of direct measurements did not exceed 1.5 $\times$ 10^6 Cells L^{-1} and only a few spectra related to the case of $N_{\text{coc}} > 5 \times 10^6$ Cells L^{-1}. When deriving the algorithm, differences in $N_{\text{cl}}/N_{\text{cc}}$ for different years were not taken into account. However, it was possible to identify a set of data for which the b_{bp} correlated well with the a_{g} coefficient (R^2 = 0.82). This allowed us to reliably take into account the contribution of terrigenous suspension and not show 'false' coccolithophore blooms in the area of strong influence of river runoff.

In our work, we used the approach of the algorithm presented in [29], but tried to use other values for its parameters K_{coc}, K_{riv}, and $b_{\text{bp\_bg}}$ in order to improve its accuracy in conditions of intense coccolithophore bloom, which was observed in 2017 and 2022.

For the 2017 and 2022 dataset, the coefficient of determination R^2 for the linear correlation between b_{bp} and a_{g} is 0.60, which indicates less influence of terrigenous suspended matter in these years. Therefore, reduction by multiple times was considered for the K_{riv} and $b_{\text{bp\_bg}}$ parameters.

2.5. Error Assessment

To evaluate the accuracy of the N_{coc} algorithm and remote sensing reflectance values, the root mean square error (RMSE) and mean absolute percentage error (MAPE) were calculated as

$$\text{RMSE} = \sqrt{\frac{1}{N} \sum_{i=1}^{N} (y_i - y_i^m)^2}, \tag{6}$$

$$\text{MAPE} = \frac{1}{N} \sum_{i=1}^{N} 100\% \cdot |y_i - y_i^m| / y_i^m, \tag{7}$$

where y_i and y_i^m are the calculated and measured values of coccolithophore concentrations or remote sensing reflectance.

The regional N_{coc} estimation algorithm uses two spectral bands in the range of 486–489 and 551–556 nm. For the 2022 stations, when in situ measurements of $R_{\text{rs}}(\lambda)$ were carried out, estimates of the correspondence of satellite and in situ R_{rs} values in spectral bands from the considered spectral ranges were made. For a set with satellite data on the same day (16 pairs in total), the maximum difference for MODIS and VIIRS-JPSS for both bands did not exceed 8%, and MAPE was equal to 4%. With an increase in the permissible time difference between satellite and shipboard measurements to 32 h (37 pairs), the maximum

difference reached 60%, and MAPE turned out to be equal to 15% for MODIS and 8–9% for VIIRS-JPSS. Our estimates of the differences between satellite and in situ R_{rs} values during the CB period are even slightly better than those obtained in earlier work [57], where for the VIIRS-JPSS band 556 nm, MAPE = 9.3%, and for the 555 nm band of two MODIS sensors, MAPE was equal to 10.3 and 12.3%, respectively. It is worth noting that [57] used a dataset with more spectra and a time difference between in situ and satellite measurements less than 2 h, as waters were strongly influenced by river runoff.

The acceptable difference between the satellite and in situ R_{rs} allowed us to use the combined set of satellite and in situ R_{rs} spectra to modify the regional N_{coc} estimation algorithm.

2.6. Tuning of the Hydrolight Model

Hydrolight software was used to calculate the light field parameters. We used the case 2 water model, where inherent optical properties were determined for 4 components [58]. The parameters of pure water absorption and scattering were taken from [59,60].

The optical properties of the component associated with *Chl* were parameterized through its concentration. The result of field measurements of the concentration of *Chl* at the depths of 1–10 m shows insignificant (5–10%) changes, so the concentration was set as a constant with depth. Absorption and scattering parameters were introduced using standard models available in Hydrolight [61,62]. The parameters of the scattering phase function represent the Morel model for "large particles" [63].

The CDOM component was considered to be non-scattering. The absorption of CDOM was calculated relatively to the absorption value at wavelength 443 nm $a_g(443)$ [56]. This value and CDOM spectral slope were specified using the results of laboratory ICAM measurements, or through the GIOP $R_{rs}(\lambda)$ decomposition algorithm [64].

The mineral suspension component was set, assuming that the suspension is represented only by coccolithophore cells and detached coccoliths, which corresponds to more than 99% of the biomass during intense blooms, according to in situ measurements. The absorption properties of coccolithophores and coccoliths were neglected, as they are several times less than those of *Chl* and CDOM. We used the typical coccolithophore bloom backscattering ratio value $b_b/b = 0.02$ [65], and the spectral scattering coefficient $b(\lambda)$ was assigned as

$$b(\lambda) = b_0 \, (550/\lambda)^m. \tag{8}$$

The parameters b_0 and m were determined to spectrum $b_b(\lambda)$ and matched the results of the decomposition of the R_{rs} spectra using GIOP. The depth of a homogeneous surface layer with coccolithophores Z_{coc} was also specified, below which coccolithophore concentration was set to zero.

Figure 2a shows the comparison of the scattering parameters b_0 and m calculated using GIOP from satellite and in situ R_{rs} (λ) spectra. In this case, all available satellite spectra were used. The coefficient of determination R^2 of the linear correlation was 0.49, which made it possible to determine the parameter m based on the value b_0:

$$m = 1.274 - 0.067 \cdot b_0 \tag{9}$$

Parameter b_0 correlates well with the concentration of N_{cc_cl} according to direct measurements ($b_0 = 0.207 \cdot N_{cc\_cl}$, $R^2 = 0.62$, Figure 2b). Only satellite spectra with a measurement time difference of less than 8 h were used here. If we expand the array of satellite data by increasing the time interval to 32 h, then R^2 will decrease to 0.49, and the correlation equation will change slightly: $b_0 = 0.212 \cdot N_{cc\_cl}$. However, as can be seen in Figure 2b, there is a significant difference in the location of the data for 2017 and 2022 relative to the regression line for the general dataset, which can be explained by the different phases of blooms recorded according to in situ measurements over these years. If we calculate the regression separately for each year, then for 2017, we will obtain $b_0 = 0.245 \cdot N_{cc\_cl}$, and for 2022, it will be $b_0 = 0.145 \cdot N_{cc\_cl}$.
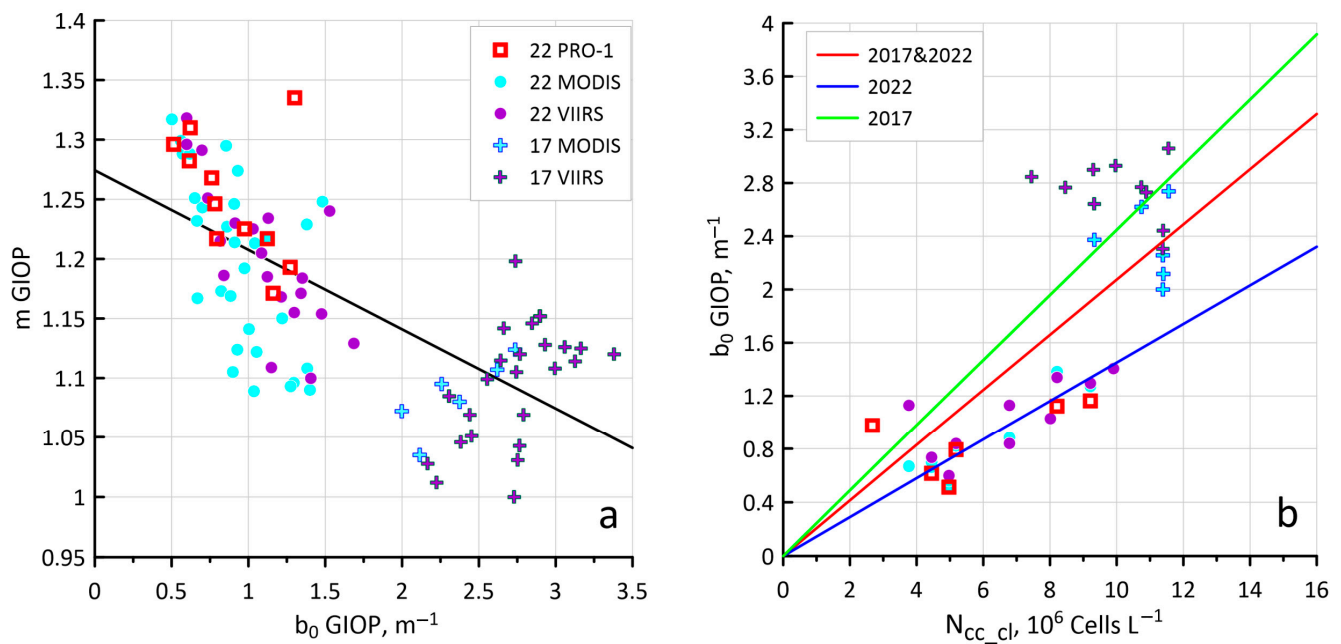
Figure 2. Comparison of scattering parameters and concentration of coccolithophores: (**a**) parameters b_0 and m for coccolithophore backscattering, calculated by GIOP; (**b**) coefficient b_0 and concentration N_{cc_cl}. Solid straight lines are linear regressions.

3. Results

3.1. Coccolithophore Concentrations in the Northeastern Part of the Black Sea in 2017 and 2022

In 2017, intense coccolithophore bloom represented by one species *Emiliania huxleyi* was observed at all stations from the shelf to stations above the depth of 1500 m. The maximum number of coccolithophores exceeded 9×10^6 Cells L^{-1} (Table S1), and their contribution to the total phytoplankton biomass was above 99%. Coccolithophore bloom was observed mainly in the upper mixed layer. The median concentration of coccolithophore cells for all sampling depths was equal to 6×10^6 Cells L^{-1}, and for the two upper ones was 7×10^6 Cells L^{-1}.

In 2022, coccolithophore bloom was generally less intense, although the abnormally high value of 13×10^6 Cells L^{-1} was obtained at one station (Table S2). Bloom also occurred at all stations of the continental shelf and slope, and it was recorded in the upper mixed layer. The median concentration of coccolithophore cells for all sampling depths was equal to 4×10^6 Cells L^{-1}, and for the two upper ones was 5.4×10^6 Cells L^{-1}.

The median value for the N_{cl}/N_{cc} ratio for all sampling depths in 2017 was 11.5, and for the two upper ones was 15.0; in 2022, for all depths it was 1.3, and for the two upper ones was 2.2. Such a strong difference in the value of N_{cl}/N_{cc}, apparently, occurs due to the difference in the bloom phase for those two years. In June 2022, the bloom was in an earlier phase, when significantly fewer detached coccoliths were observed; in June 2017, measurements were performed near the end of bloom, so the abundance of detached coccoliths exceeded the abundance of placed coccolithophore cells.

3.2. Sensitivity of the N_{coc} Algorithm to Variations in Bio-Optical Characteristics

Figure 3 shows a comparison of the measured and model $R_{rs}(\lambda)$ spectra using the examples of station 1_22 (11.06.2022, 44.56N, 37.96E) and station 3_17 (08.06.2017, 44.48N, 37.85E). For station 1_22, the model spectra are compared with the field-measured $R_{rs}(\lambda)$, and for station 3_17, with the spectrum according to MODIS Terra data. The concentration of N_{cc_cl} according to direct measurements for station 1_22 was 5.2×10^6 Cells L^{-1}, and for station 3_17 was 11.6×10^6 Cells L^{-1}. In this case, for station 1_22, the best agreement of the model spectrum with the measured one was achieved for $Z_{coc} = 10$ m, while in the case

of more intense bloom at the station 3_17, the spectrum matched for Z_{coc} = 5 m. For both stations, the value of Z_{coc}* was calculated, when all model spectra with $Z_{coc} > Z_{coc}$* hardly differed from the one obtained with Z_{coc}*. This indicates that the $R_{rs}(\lambda)$ spectrum is formed by the upper layer of a water column with a thickness of Z_{coc}*. For the stations shown in Figure 3, the Z_{coc}* was 15 and 10 m.
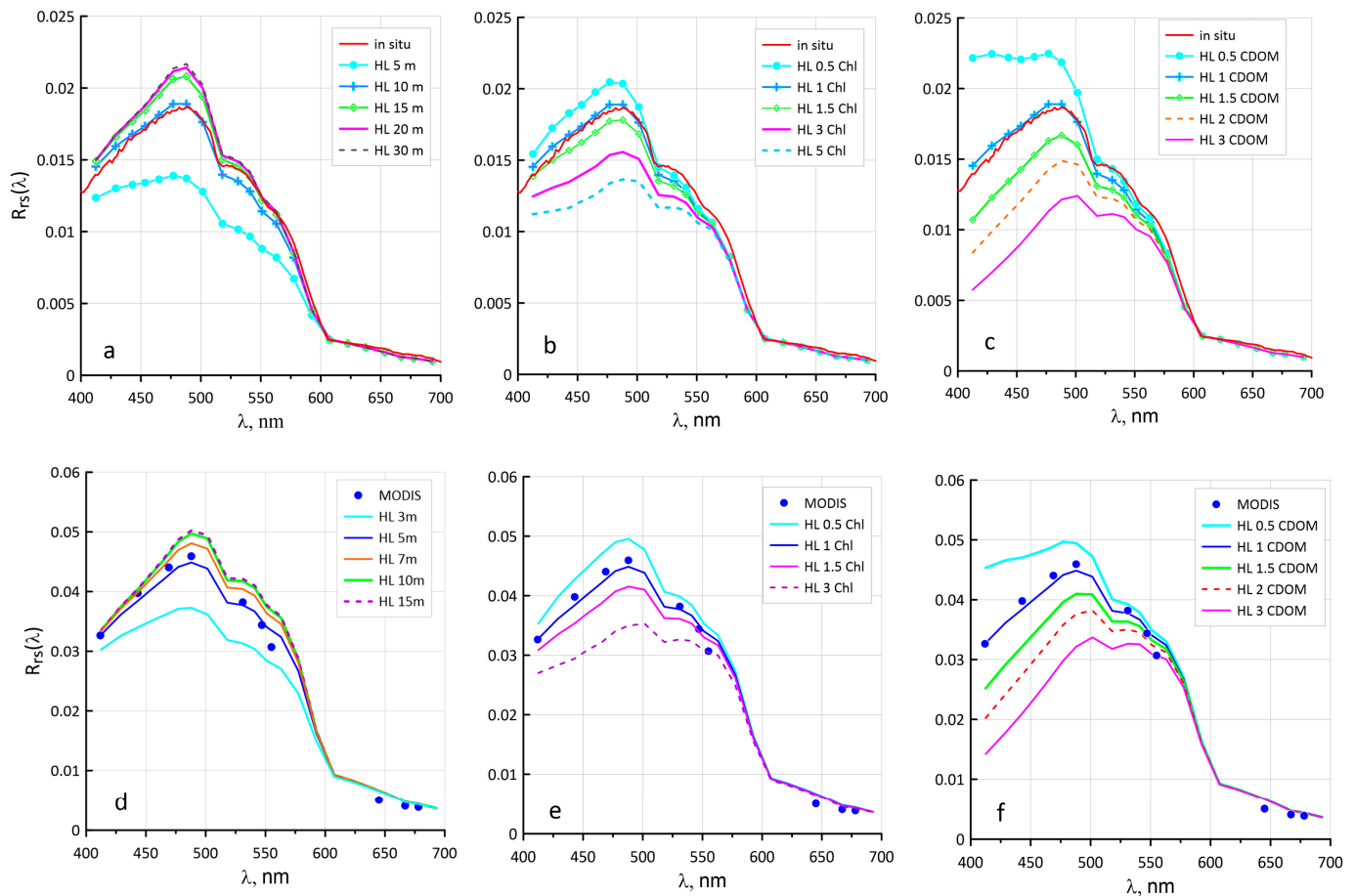

Figure 3. The results of modeling the $R_{rs}(\lambda)$ spectra with Hydrolight software with a change in the values of Z_{coc} (**a**,**d**), *Chl* (**b**,**e**), and CDOM (**c**,**f**) using data from stations 1_22 (upper row) and 3_17 (bottom row). The notation Chl/CDOM 'X' refers to the case of an X-fold increase in the concentration of *Chl* or $a_g(443)$.

To test the stability of the regional coccolithophore concentration algorithm to variations in the *Chl* concentration and the CDOM content, additional model calculations were carried out (Figure 3 in the center and right column). These variations were set using a multiplier X to the initial values of *Chl* and $a_g(443)$, for which the best agreement was obtained with the measured R_{rs} spectra. The effect on the R_{rs} spectrum of the change in CDOM is more noticeable than the change in *Chl* (Figure 3). The reason for this is that the CDOM-related absorption is usually significantly greater than the phytoplankton absorption in the northeastern part of the Black Sea. When the *Chl* value changes by 50%, there is only a slight change in the $R_{rs}(\lambda)$ spectra, while the same relative decrease in CDOM brings not only a significant increase in R_{rs}, but also a noticeable change in the shape of the spectrum. This shape is typical for coccolithophore bloom spectra in the Barents Sea [66], where the content of CDOM is significantly lower than in the Black Sea. Only with such a low content of CDOM or with a significant increase in *Chl* (3–5 times) is the effect of the maximum absorption by phytoplankton near 450 nm noticeable in the shape of a small deflection of the $R_{rs}(\lambda)$ spectrum near this wavelength.

Table 1 shows the sensitivity of the regional N_{coc} algorithm [29] to variations in the Z_{coc}, *Chl*, and the absorption of CDOM values. In addition to the N_{coc} values for different model spectra (Figure 3), their difference (Δ, %) from the N_{coc}* values calculated from the measured spectra (N_{coc}* = 3.1 and 13.4 $\times$ 10^6 Cells L^{-1} for station 1_22 and 3_17, respectively) is shown. A decrease in Z_{coc} by 2 times leads to underestimation of N_{coc} estimates by almost 2 times for station 1_22, where the bloom is not so intense. For station 3_17, with a decrease in Z_{coc}, there is also a significant decrease in N_{coc} (by more than 3×10^6 Cells L^{-1}, ~26%). The increase in Z_{coc} does not play such a significant role, since the spectrum of upwelling radiation is formed by the surface layer of the water column—Z_{coc}*. In fact, a greater relative variability of N_{coc} estimates in response to changes in modeling parameters was observed for station 1_22, with a less intense CB than for station 3_17. The N_{coc} for station 1_22 changes particularly noticeably when the CDOM absorption changes. For station 3_17, in an intense CB area, the response to changes in CDOM and *Chl* is approximately the same, as the absorption of *Chl* becomes comparable to the absorption of CDOM for the 488 nm spectral band used in the N_{coc} algorithm. The higher concentration of *Chl* (0.47 in comparison to 0.2 mg L^{-1}) proves it, while the value of CDOM for station 3_17 is only 26% higher than station 1_22.

Table 1. The values of N_{coc} (10^6 Cells L^{-1}) according to the 2014 algorithm [29] and their difference Δ (%) from the values of N_{coc}* calculated from the measured spectra, depending on the parameters of the Hydrolight model with an example for stations 1_22 and 3_17. Columns highlighted in bold refer to calculations with the set of parameters when the best match between the measured and calculated R_{rs} spectra was obtained.

	St. 1_22				St. 3_17			
Z_{coc}	5	**10**	15	20	3	**5**	7	10
N_{coc}	1.4	**3.1**	3.6	3.8	11.0	**14.3**	15.7	16.4
Δ	−53%	**1%**	19%	24%	−16%	**10%**	21%	26%
X * *Chl*	0.5	**1**	1.5	3	0.5	**1**	1.5	3
N_{coc}	3.5	**3.1**	2.8	2.0	15.2	**14.3**	13.6	11.8
Δ	14%	**1%**	−10%	−36%	17%	**10%**	4%	−9%
X CDOM	0.5	**1**	1.5	2	0.5	**1**	1.5	2
N_{coc}	3.8	**3.1**	2.4	1.7	15.0	**14.3**	13.6	12.9
Δ	25%	**1%**	−22%	−45%	15%	**10%**	5%	−1%

* The notation 'X' refers to the case of an X-fold increase in the concentration of *Chl* or $a_g(443)$.

3.3. New Values of K_{coc} as a Result of Hydrolight Modeling

Using a customized bio-optical model, R_{rs} calculations were carried out for five values of N_{cc_cl} 2, 4, 7, 10, and 15 $\times$ 10^6 Cells L^{-1}. For each value of the concentration of N_{cc_cl}, the values of *Chl* (0.3, 0.5, and 0.8 mg L^{-1}) and CDOM (0.03, 0.05, and 0.08 m^{-1}) were varied to cover the most likely range of changes in these optically active components (OAC), typical for the northeastern part of the Black Sea [55,67]. The calculations were carried out under the assumption of a homogeneous distribution of coccolithophores in the layer 15 m deep, which generally corresponds to the results of the performed field measurements of the vertical profiles of the beam attenuation coefficient $c(530)$.

Thus, 45 R_{rs} spectra were obtained, to which the regional algorithm was applied to estimate the N_{coc} concentration. The comparison of the N_{cc_cl} input values used in Hydrolight calculations and obtained N_{coc} estimates is shown in Figure 4. If we use the values of the parameters K_{coc}, K_{riv}, and b_{bp_bg} defined in the article [29], then the N_{coc} estimates (shown in pink circles) vary visibly in response to changes in the content of the OAC. Simultaneously, overestimated N_{coc} evaluations are obtained for N_{cc_cl} = 15 $\times$ 10^6 Cells L^{-1}, and underestimated ones (in a number of cases even negative) for N_{cc_cl} = 2 $\times$ 10^6 Cells L^{-1}. This result arises from the fact that in our Hydrolight model, the contribution of terrigenous

suspended matter is not taken into account. The origin of this matter is associated with river runoff, as well as with the b_{bp} background amount, which is parametrized through the b_{bp_bg} value. Therefore, N_{coc} estimates were calculated for the case of $K_{riv} = 0$ and $b_{bp\_bg} = 0$ (blue circles in Figure 4). In this case, the influence of the OAC practically disappears, but for all N_{cc_cl} data, overestimated N_{coc} values are obtained, and this overestimation increases in direct proportion to N_{cc_cl}, which indicates an incorrect K_{coc} value. For the best correspondence of the initial values N_{cc_cl} with the results of N_{coc} estimates, the value 4.36×10^{-3} is used (red circles in Figure 4).
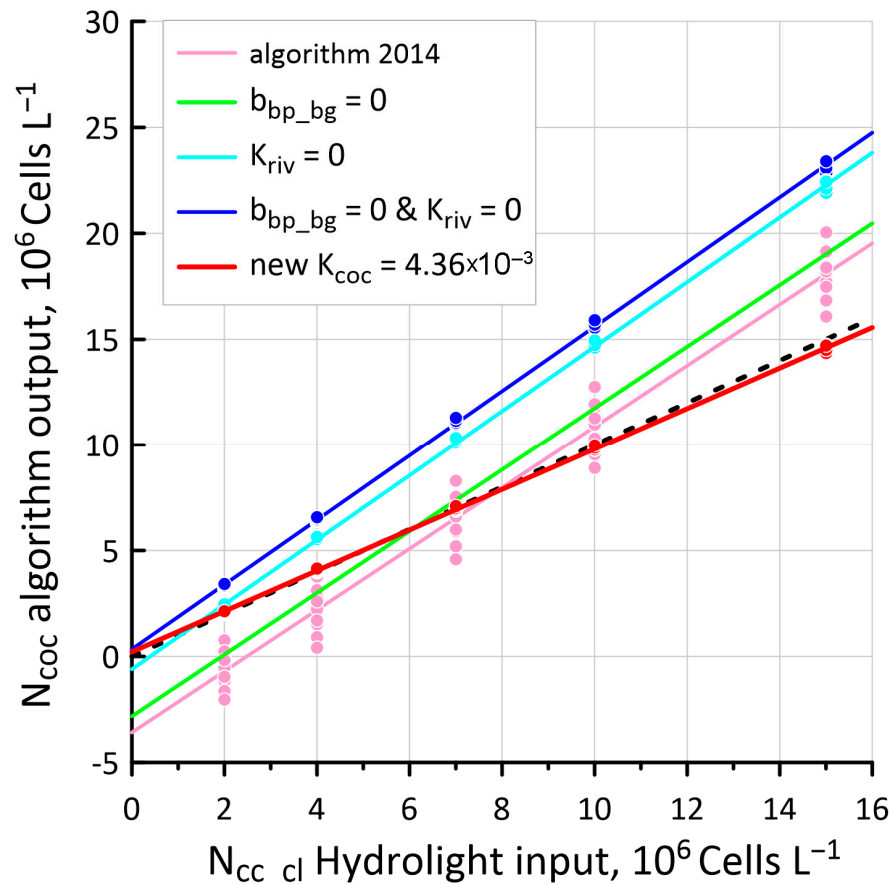
Figure 4. Comparison of N_{cc_cl} input values used in Hydrolight calculations and the N_{coc} estimates obtained depending on the regional algorithm parameters. The circles show individual calculations, solid lines show linear regressions, and the dotted line shows a perfect 1:1 correspondence.

Figure 4 also shows N_{coc} estimates for the cases of $K_{riv} = 0$ (in blue) and $b_{bp\_bg} = 0$ (in green). The results obtained in these cases are close to the variants of $K_{riv} = 0$ and $b_{bp\_bg} = 0$ and the original algorithm [29], respectively, showing that the influence of the value of b_{bp_bg} on the algorithm results is significantly less than the influence of K_{riv}.

As was previously noted (Section 2.4), there are noticeable differences for the data we use depending on the year. Therefore, similar calculations of R_{rs} spectra arrays were performed, but using the coupling equations between b_0 and N_{cc_cl} obtained separately for 2017 and 2022 data. These arrays allowed us to obtain two more variants of the K_{coc} value: 5.13×10^{-3} for 2017 and 3.10×10^{-3} for 2022. Additionally, if the first K_{coc} value is almost two times higher than the previous K_{coc} estimate [29], then the second one is very close to it. The use of these K_{coc} values is discussed in Sections 3.4 and 4.5.

3.4. Configuring Other Model Parameters

As long as the results of the Hydrolight calculations were obtained without taking into account the terrigenous suspended matter, the presence of which is quite possible when using real data, the data of in situ and satellite measurements of R_{rs} were used to adjust two parameters of the N_{coc} algorithm related to the terrigenous suspended matter (K_{riv} and b_{bp_bg}) for stations where the in situ measurements of N_{cc_cl} were completed. The difference in measurement time between satellite and shipboard data did not exceed 8 h. In total, 41 corresponding spectra were selected for 2017 and 2022.

We set the value of K_{riv} and b_{bp_bg} as a fraction of their values defined in the previous work [29], leaving values from the original algorithm or decreasing them. For example, the notation '0.25_0.5' means that $K_{riv} = 0.25 \times 0.157 = 0.03926$ and $b_{bp\_bg} = 0.5 \times 0.0025 = 0.00125$.

For the K_{coc} parameter, both previous values 2.74×10^{-3} and three new variants, 3.10, 4.36, and 5.13×10^{-3}, obtained in Section 3.3 were used. As there is a rather large difference between the variants of the K_{coc} 3.10 and 4.36×10^{-3}, two more intermediate ones were used: 3.52 and 3.94×10^{-3}. Table 2 shows the RMSE and MAPE values of the N_{coc} estimates obtained relative to the measured N_{cc_cl} for the selected dataset and depending on the three parameters values of the algorithm: K_{coc}, K_{riv}, and b_{bp_bg}.

Table 2. The RMSE (10^6 Cells L^{-1}) and MAPE values of N_{coc} estimates relative to the measured N_{cc_cl} for the selected dataset and depending on the value of the parameters of the algorithm K_{coc}, K_{riv}, and b_{bp_bg}.

K_{riv} and b_{bp_bg} *	1.0_1.0	1.0_0.5	0.5_1.0	0.5_0.5	0.25_1.0	0.25_0.5	0.1_0.1
$K_{coc}\ 10^3$				RMSE			
2.74	2.68 **	2.57	2.70	2.77	2.90	3.05	3.47
3.1	2.75	2.54	2.40	2.32	2.37	2.37	2.56
3.52	3.08	2.82	2.52	2.32	2.31	2.16	2.06
3.94	3.46	3.21	2.85	2.61	2.57	2.35	2.08
4.36	3.83	3.59	3.23	2.99	2.93	2.69	2.35
5.13	4.41	4.19	3.86	3.64	3.57	3.35	3.01
$K_{coc}\ 10^3$				MAPE			
2.74	35%	32%	31%	29%	30%	29%	32%
3.1	36%	33%	31%	29%	29%	27%	25%
3.52	39%	36%	32%	30%	30%	28%	25%
3.94	43%	40%	36%	33%	33%	30%	26%
4.36	48%	45%	40%	37%	37%	34%	29%
5.13	55%	52%	48%	45%	44%	41%	37%

* The values of K_{riv} and b_{bp_bg} are given as fractions of their values determined in the previous work [29]. ** The underlined values of RMSE and MAPE correspond to the algorithm parameters that were used in Figure 5.

If we focus on the RMSE and MAPE values, the best correspondence between the calculated N_{coc} and the measured N_{cc_cl} is obtained in the case of 0.1_0.1 and $K_{coc} = 3.52 \times 10^{-3}$. In fact, it is the option of reducing the contribution of terrigenous suspended matter to 10% of the initial one, almost regardless of the K_{coc} value, that leads to a decrease in RMSE and MAPE and, therefore, to an improvement in compliance. Comparison graphs of N_{coc} vs. N_{cc_cl} show that the discrepancy in the variants with different values of the algorithm parameters are no longer so noticeable (Figure 5). The best option, "10%" (Figure 5b), does not differ much from the original "algorithm 2014" (Figure 5a); it even has less difference from the intermediate "50%" option (Figure 5c), although the values of RMSE and MAPE are noticeably different for all given versions.
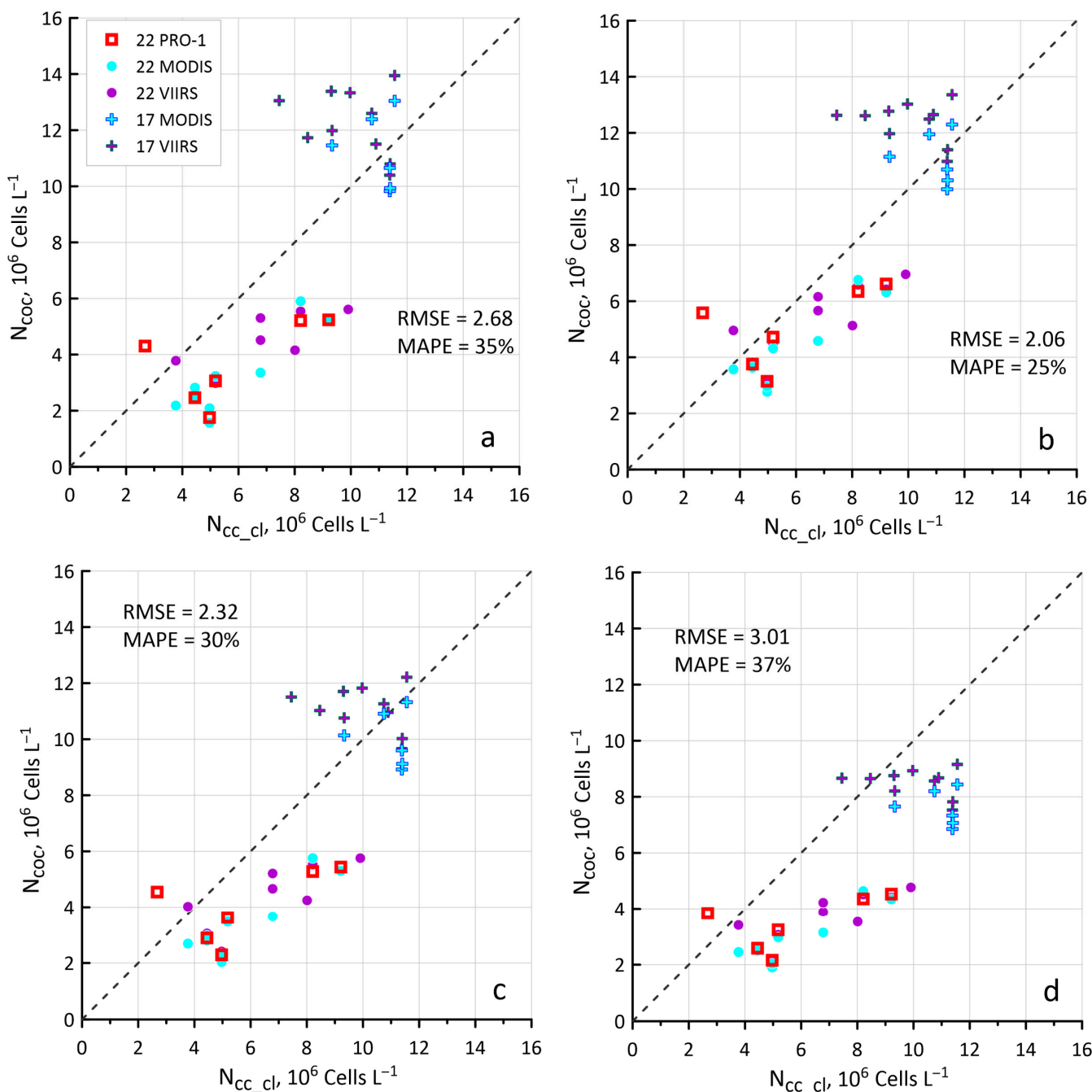
Figure 5. Comparison of the coccolithophore concentration N_{coc} calculated from $R_{rs}(\lambda)$ with different parameters of the regional algorithm K_{coc}, K_{riv}, and b_{bp_bg}, and measured N_{cc_cl}: (**a**) algorithm 2014 (1.0_1.0, $K_{riv} = 2.74 \times 10^{-3}$); (**b**) option "10%" (0.1_0.1, $K_{riv} = 3.52 \times 10^{-3}$); (**c**) option "50%" (0.5_0.5, $K_{riv} = 3.52 \times 10^{-3}$); (**d**) option "10% 2017" (0.1_0.1, $K_{riv} = 5.13 \times 10^{-3}$). Notations are the same as in Figure 2.

Figure 5d shows the variant 0.1_0.1 and $K_{coc} = 5.13 \times 10^{-3}$, as it was the value of K_{coc} obtained in the Hydrolight calculations with the focus on 2017 data and the corresponding best option for terrigenous suspended matter was selected from Table 2. However, even if we only pay attention to the data for 2017, the "50%" option suits them much better (Figure 5c). Thus, model calculations do not always allow us to find the best variant of the algorithm parameters that works with real satellite data, because atmospheric correction errors begin to contribute to the accuracy of the latter [57,68], as well as errors associated

with the time difference between in situ and satellite measurements. In addition, the error is caused by the discrepancy between the spatial resolution of shipboard and satellite data and the interannual dynamics of phytoplankton communities.

Furthermore, we will consider the "10%" option (0.1_0.1 and $K_{coc} = 3.52 \times 10^{-3}$) to be the best one for the conditions of intensive CB in the northeastern part of the Black Sea. We will denote it as 'algorithm 2023'. The algorithm code (MATLAB script) for both algorithms (2014 and 2023) is available in the Supplementary Materials.

4. Discussion

4.1. Coccolithophore Blooms in the Black Sea

Coccolithophore blooms are an almost annual phenomena in the Black Sea, but in 2017 and 2022, these blooms reached their maximum intensity in comparison to previous years [28]. The maximum concentration of *Emiliania huxleyi* was registered in 2022, and it has been the maximum for all the years of research since the beginning of this century. Coccolithophore blooms grow in the upper mixed layer with high stability of the water column [22]. In the northeastern part of the Black Sea, weak SE winds dominate in late and early spring, and wind forcing during this period is minimal [28,69]. This contributes to the development of a sharp seasonal thermocline, the presence of which is a necessary condition for the bloom [22,24,28,70].

Typical features of the blooms of 2017 and 2022 are the presence of a large number of detached coccoliths (Tables S1 and S2). In 2017, the number of detached coccoliths per *Emiliania huxleyi* plated cell reached 600. In 2022, this number was lower, but still high. This suggests that the bloom was in late phase and the number of destroyed cells accumulated. One of the possible mechanisms for the appearance of a large number of detached coccoliths during the bloom is the intensive consumption of living cells by species of a higher trophic level [71].

Due to a large number of plated cells and detached coccoliths in the upper mixed layer, a kind of optical medium is created to generate optimal conditions for the growth of coccolithophore cells, and does not allow other species in competition to win [65]. However, it is not yet clear why intense coccolithophore blooms grow. There is a hypothesis that the intensity of blooms is related to the nature of winters, as after cold winters, there are usually more intense blooms [70,72]. However, the details of this connection remain unclear.

4.2. Sensitivity of the New N_{coc} Algorithm

Table 3 shows the sensitivity test results of the 2023 regional algorithm to determine N_{coc} with the example of the 1_22 and 3_17 stations (just as in Table 1). Firstly, the new algorithm has allowed us to obtain N_{coc}* estimates from the measured spectra that better correspond to the data of direct measurements of N_{cc_cl}. For the station 1_22, N_{coc}* = 4.7 $\times$ 10^6 Cells L^{-1}, and for 3_17 it is 12.3 $\times$ 10^6 Cells L^{-1}, which is much closer to the estimates of N_{cc_cl}: 5.2 and 11.6 $\times$ 10^6 Cells L^{-1}, respectively. Secondly, the new algorithm has become significantly less sensitive to *Chl* and CDOM value changes, which is a consequence of a reduction in the contribution of terrigenous suspended matter to the total suspension matter backscattering. With a 50% change in *Chl* and CDOM, the N_{coc} estimates for both stations now hardly change. The influence of the Z_{coc} layer thickness has somewhat decreased, but the mechanism of this influence remains the same.

Table 3. The values of N_{coc} (10^6 Cells L^{-1}) according to the algorithm "10%" and their difference Δ (%) from the value of N_{coc}* calculated from the measured spectra, depending on the parameters of the HydroLight model for the stations 1_22 and 3_17. Columns highlighted in bold refer to calculations with a set of the parameters when the best match between the measured and calculated R_{rs} spectra was obtained.

	St. 1_22				St. 3_17			
Z_{coc}	5	**10**	15	20	3	**5**	7	10
N_{coc}	3.3	**4.2**	4.5	4.5	11.7	**14.1**	15.1	15.6
Δ	−30%	**−10%**	−5%	−4%	−5%	**15%**	23%	27%
X * Chl	0.5	**1**	1.5	3	0.5	**1**	1.5	3
N_{coc}	4.23	**4.23**	4.24	4.24	14.2	**14.1**	14.0	13.8
Δ	−10%	**−10%**	−10%	−10%	16%	**15%**	14%	12%
X CDOM	0.5	**1**	1.5	2	0.5	**1**	1.5	2
N_{coc}	4.27	**4.23**	4.20	4.16	14.0	**14.1**	14.3	14.4
Δ	−10%	**−10%**	−11%	−12%	−5%	**15%**	15%	23%

* The notation 'X' refers to the case of an X-fold increase in the concentration of *Chl* or a_g(443).

4.3. Comparison of N_{coc} Distributions for 2014 and 2023 Algorithms

Figure 6 shows a comparison of the distributions of N_{coc} concentration estimates calculated with the old [29] and the new 2023 algorithms for the entire Black Sea. For this figure, we used data from two VIIRS overpasses for 12 June 2017 and 17 June 2022, which gives us an opportunity to see almost the entire Black Sea water area and relate to the time of the expeditions in those years. For both images, the comparison of the two algorithms shows that the main difference between their results arises primarily in areas affected by river runoff: for example, near the mouth of the Danube River or in the Sea of Azov. There are also noticeable differences in the area of low N_{coc} concentrations. This is especially noticeable for 2022 in the central part of the sea, where according to the 2014 algorithm, there was no CB; However, the modified algorithm indicates its presence ($N_{coc} > 10^6$ Cells L^{-1}).

In addition, Figure 6 shows the differences in CB in the studied years. In 2017, intensive CB with $N_{coc} > 4 \times 10^6$ Cells L^{-1} covers almost the entire Black Sea area (with the exception of the northwestern shelf area). In 2022, extremely high values of $N_{coc} > 15 \times 10^6$ Cells L^{-1} were observed near the northeastern coast, but for the rest of the Black Sea, the CB was less intensive or absent.

Since the modification of the N_{coc} algorithm in conditions of intense CB has been carried out on the basis of field measurement data in a fairly small area in the northeastern part of the Black Sea, the new algorithm may not be suitable for the entire sea. The informative MODIS Terra data from 8 June 2017 were selected to see the differences between the two algorithms' performance in the eastern part of the sea (Figure 7). Note that a different scale was chosen. As there are no rivers as large as the Danube or Dnieper in the eastern part of the sea, the differences between the two algorithms appear only in the area of relatively small N_{coc} values. In addition, it is worth noting that despite a very intense CB near the northeast coast in 2022, satellite N_{coc} values were clearly lower in the sampling area near Gelendzhik than those from 2017. Thus, the differences for satellite estimates of the CB near Gelendzhik are consistent with the field measurement data.
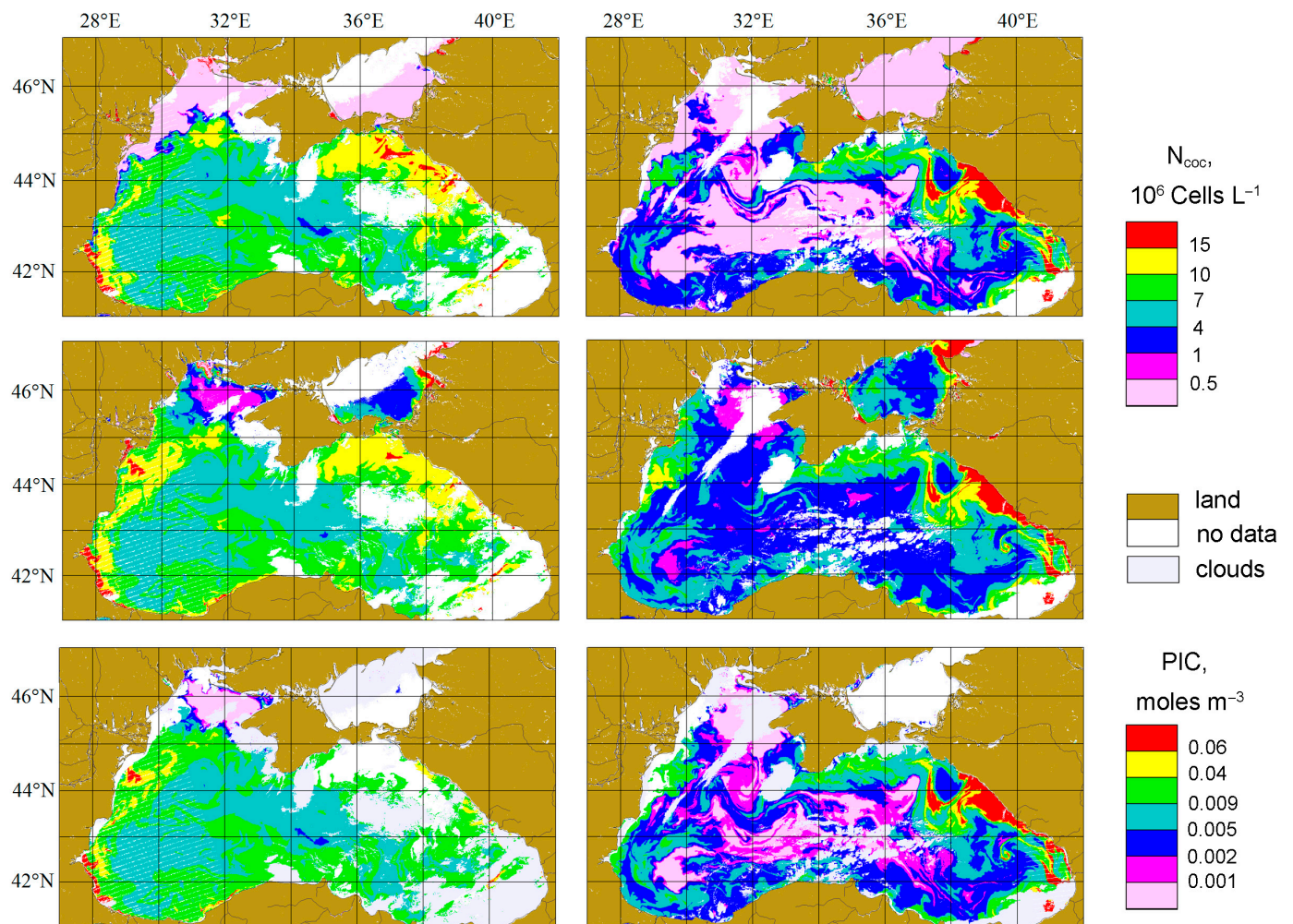
Figure 6. Spatial distributions of N_{coc} in the Black Sea, calculated with 2014 and 2023 algorithms (upper and middle rows), and PIC (lower row). On the **left** are VIIRS data from 12 June 2017, and on the **right** are VIIRS data from 17 June 2022.

Thus, the new algorithm gives more accurate estimates in conditions of intense CB and the absence of strong influence of terrigenous suspended matter. However, for areas affected by significant river runoff and in areas of weak CB ($N_{coc} < 3 \times 10^6$ Cells L^{-1}), it seems that the previous version of the algorithm should be used. To set up a regional algorithm in such waters, it is necessary to conduct complex expedition studies, including in situ determination of the coccolithophore concentration. Note that spectral variations of the remote sensing reflectance during coccolithophore blooms in the western part of the Black Sea, affected by river runoff, were carried out in [57] according to AERONET-OC. Nevertheless, the authors did not have in situ data on the coccolithophore concentration, although it is typical for a number of other works [73–77], due to the complexity of such measurements.
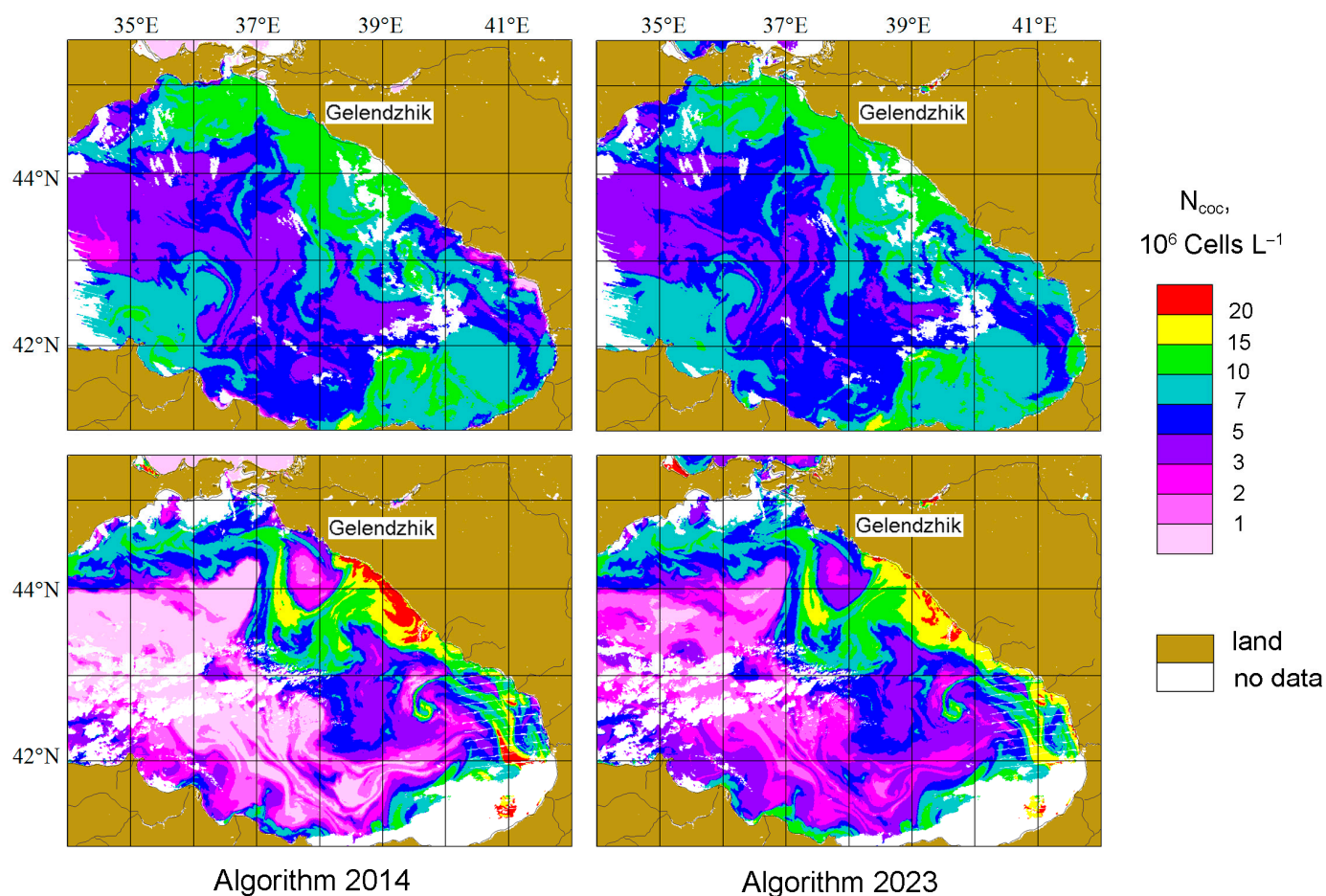
Figure 7. Comparison N_{coc} spatial distributions in the eastern part of the Black Sea, calculated with the 2014 and the new 2023 algorithms. **Upper row**: MODIS Terra data from 6 August 2017, **lower row**: VIIRS data from 17 June 2022.

4.4. The Comparison with PIC Product

The standard satellite data processing product particle inorganic carbon (PIC) is widely used for CB intensity and calcite ($CaCO_3$) concentration assessments [78,79]. In the work [29], an equation of the relationship between N_{coc} and PIC with a correlation coefficient of 0.61 was obtained. The comparison of the distributions of N_{coc} and PIC for two satellite overpasses with intensive CB in June 2017 and 2022 is shown in Figure 6. It can be seen that, in fact, the N_{coc} and PIC distributions are visually similar. Note that for PIC values in areas affected by river runoff (for example, near the mouth of the Danube River) the data are masked, while the 2014 algorithm yields low N_{coc} estimates in these areas. Moreover, sometimes, areas where the algorithm for N_{coc} shows an intense CB are hidden in PIC distribution map, as was the case near the Kerch Strait (45N, 37E) for the 2017 image, for example.

According to the 8 June 2017 MODIS Terra data in the eastern part of the Black Sea (Figure 7 upper image), the pixel-by-pixel comparison of PIC and N_{coc} values was performed for both N_{coc} algorithms. The proportionality coefficients between N_{coc} and PIC transpired to be 252 and 250, which is quite consistent with the previous value of 223 [29]. It is of interest to make comparisons under non-typical Saharan dust transfer conditions, for which additional data correction is recommended [80].

4.5. The Effect of the Bloom Phase (The Difference for Two Years)

To select the best algorithm for estimating N_{coc} in conditions of intensive CB in the north-eastern part of the Black Sea, we focused on the correspondence of the measured and calculated N_{coc} values for the total dataset for two years. Moreover, it was seen that, on the whole, the data in these years have their own peculiarities (see Figure 5). In addition, according to direct measurements, a different ratio was recorded for them between the concentrations of placed coccolithophore cells N_{cc} and detached coccoliths N_{cl}, which may be the result of a different bloom phase during field measurements. In order to select the best algorithm for each year separately, the statistical parameters (RMSE and MAPE) of the calculated N_{coc} and measured N_{cc_cl} are presented separately for each year (Table 4).

Table 4. The RMSE (10^6 Cells L^{-1}) and MAPE values of the N_{coc} estimates relative to the measured N_{cc_cl} for the 2017 and 2022 data separately and depending on the value of the parameters of the algorithm K_{coc}, K_{riv}, and b_{bp_bg}.

	2017			2022		
K_{riv} and b_{bp_bg}	1.0_1.0	0.5_0.5	0.1_0.1	1.0_1.0	0.5_0.5	0.1_0.1
$K_{coc\ 10^3}$			RMSE			
2.74	2.53	3.92	5.31	2.76	1.68	1.31 *
3.1	1.94	2.60	3.68	3.17	2.11	1.43
3.52	2.16	1.86	2.39	3.54	2.58	1.83
3.94	2.76	1.95	1.79	3.85	2.96	2.24
4.36	3.38	2.45	1.88	4.09	3.29	2.61
5.13	4.35	3.46	2.76	4.44	3.75	3.16
$K_{coc\ 10^3}$			MAPE			
2.74	23%	35%	50%	42%	26%	21%
3.1	16%	23%	33%	48%	33%	21%
3.52	17%	16%	21%	53%	39%	27%
3.94	22%	16%	15%	57%	44%	33%
4.36	28%	19%	15%	61%	49%	38%
5.13	38%	29%	22%	67%	55%	46%

* The underlined values of RMSE and MAPE correspond to the algorithm parameters for which the best correspondence between the calculated N_{coc} and the measured N_{cc_cl} was obtained (see text).

As in the case of a general data array, the smallest difference between the measured and calculated values was obtained with the smallest fraction of terrigenous suspension (option 0.1_0.1). Although the $K_{coc} = 3.94 \times 10^{-3}$ value suits 2017 better, for 2022, it should be changed to 2.74×10^{-3}. However, this choice is rather arbitrary as for other parameters of the algorithm almost the same compliance estimates were obtained. For example, for the 2017 data, RMSE = 1.79 and MAPE = 15% in the case of the 0.1_0.1 option and $K_{coc} = 3.94 \times 10^{-3}$, while for the 0.5_0.5 option and $K_{coc} = 3.52 \times 10^{-3}$, we obtain almost the same difference parameters: RMSE = 1.86 and MAPE = 16%. This means that although the regional algorithm can be customized for specific bloom phases, the algorithm without taking into account the bloom phase will give almost the same N_{coc} estimations equally well, which should certainly be attributed as one of its advantages. A number of previously developed optical methods can be used to detect different bloom phases [81,82].

4.6. Influence of the Spectral Index m Values for the Suspended Matter on the R_{rs} Spectra

To determine the parameter *m* of the spectral dependence of backscattering by suspended matter in HydroLight calculations, we used Equation (9) with a low coefficient of determination value ($R^2 = 0.49$). The value of *m* could vary in the range 1.0–1.3 (Figure 2). To check what effect the *m* value has on the model $R_{rs}(\lambda)$ spectrum, HydroLight calculations for station 3_17 with different values of *m* (Figure 8) were performed. It can be seen that even for extreme values of 1.0 and 1.3, the model spectra differ only very slightly. For the 551 nm band, they coincide and for 488 nm, the difference is 3%. That is, in the HydroLight

calculation model, in order to improve the N_{coc} estimation algorithm, it is possible to use Equation (9) or a fixed *m* value from the range 1.0–1.3 with good accuracy.
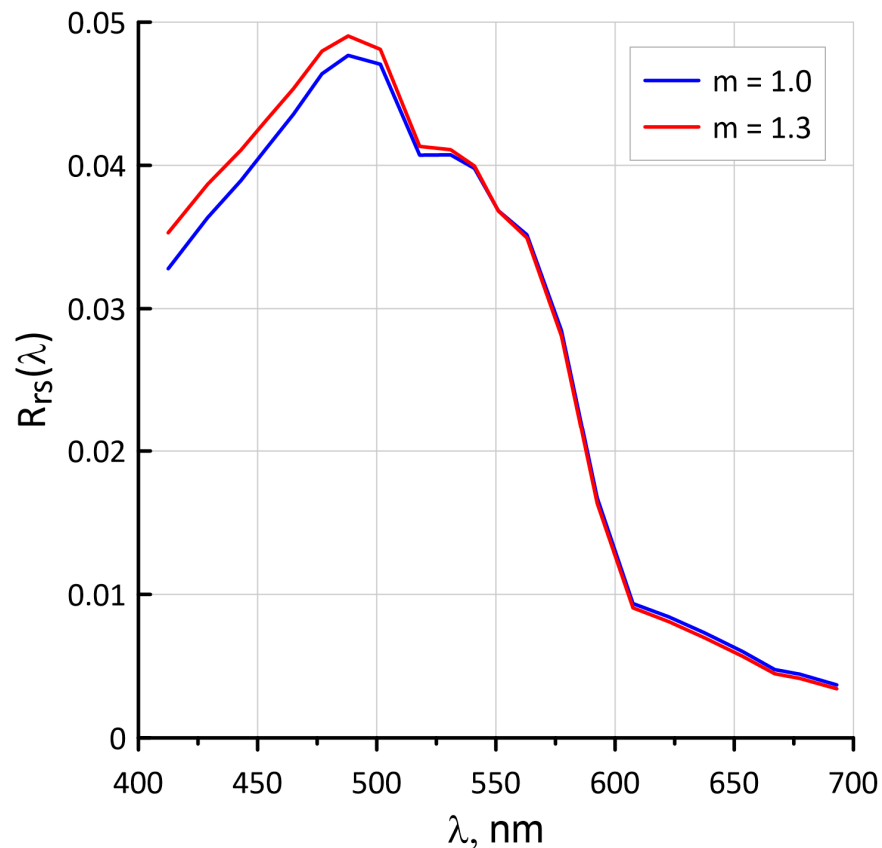

Figure 8. The results of modeling the $R_{rs}(\lambda)$ spectra using the Hydrolight software with changes in the *m* value—the parameter of the spectral dependence of suspended matter backscattering—at station 3_17.

5. Conclusions

A modified regional algorithm to quantify the concentration of coccolithophores in the northeastern part of the Black Sea under conditions of intense bloom is presented. Compared to the data underlying the previous version of the algorithm, over recent years, it has been possible to significantly expand the accumulated dataset of in situ coccolithophore and coccolith concentration determinations. In addition, the ratio between the number of detached coccoliths and plated coccolithophore cells was taken into account. The undoubted advantages of the new algorithm include its lower sensitivity to variations in the values of chlorophyll concentration and CDOM absorption, which are not associated with coccolithophorid blooms. In the future, much attention should be paid to the Western part of the Black Sea, where the problem of separating the contribution of the Danube and Dnieper rivers into the remote sensing reflectance signal arises, as well as developing an algorithm for quantifying the concentration of coccolithophorids during winter blooms. This means that it will be necessary to carry out extended expeditionary studies for the mentioned region and season, including direct determinations of the concentration of coccolithophorids. In general, the proposed approach with the separation of particulate matter into two components (terrigenous and coccolithophore) can be used to create regional or seasonal algorithms for estimating the concentration of coccolithophores in any region of the world ocean during any period. It is only necessary to have the data of field measurements of coccolithophore concentration and simultaneous shipboard or satellite measurements of the remote sensing reflectance for the selected region and period.

References

1. Field, C.B.; Behrenfeld, M.J.; Randerson, J.T.; Falkowski, P. Primary Production of the Biosphere: Integrating Terrestrial and Oceanic Components. *Science* **1998**, *281*, 237–240. [CrossRef]
2. Falkowski, P.G.; Raven, J.A. *Aquatic Photosynthesis: Second Edition*; Princeton University Press: Princeton, NJ, USA, 2013; ISBN 978-1-4008-4972-7.
3. Le Quéré, C.; Andrew, R.M.; Friedlingstein, P.; Sitch, S.; Hauck, J.; Pongratz, J.; Pickers, P.A.; Korsbakken, J.I.; Peters, G.P.; Canadell, J.G.; et al. Global Carbon Budget 2018. *Earth Syst. Sci. Data* **2018**, *10*, 2141–2194. [CrossRef]
4. Keppler, L.; Landschützer, P.; Gruber, N.; Lauvset, S.K.; Stemmler, I. Seasonal Carbon Dynamics in the Near-Global Ocean. *Glob. Biogeochem. Cycles* **2020**, *34*, e2020GB006571. [CrossRef]
5. Friedlingstein, P.; Jones, M.W.; O'Sullivan, M.; Andrew, R.M.; Bakker, D.C.E.; Hauck, J.; Le Quéré, C.; Peters, G.P.; Peters, W.; Pongratz, J.; et al. Global Carbon Budget 2021. *Earth Syst. Sci. Data* **2022**, *14*, 1917–2005. [CrossRef]
6. Volk, T.; Hoffert, M.I. Ocean Carbon Pumps: Analysis of Relative Strengths and Efficiencies in Ocean-Driven Atmospheric CO_2 Changes. In *Geophysical Monograph Series*; Sundquist, E.T., Broecker, W.S., Eds.; American Geophysical Union: Washington, DC, USA, 2013; pp. 99–110; ISBN 978-1-118-66432-2.
7. Sarmiento, J.L.; Gruber, N. *Ocean Biogeochemical Dynamics*; Princeton University Press: Princeton, NJ, USA, 2006; ISBN 978-0-691-01707-5.
8. Henson, S.A.; Sanders, R.; Madsen, E.; Morris, P.J.; Le Moigne, F.; Quartly, G.D. A Reduced Estimate of the Strength of the Ocean's Biological Carbon Pump: BIOLOGICAL CARBON PUMP STRENGTH. *Geophys. Res. Lett.* **2011**, *38*, L04606. [CrossRef]
9. Siegel, D.A.; Buesseler, K.O.; Doney, S.C.; Sailley, S.F.; Behrenfeld, M.J.; Boyd, P.W. Global Assessment of Ocean Carbon Export by Combining Satellite Observations and Food-Web Models. *Glob. Biogeochem. Cycles* **2014**, *28*, 181–196. [CrossRef]
10. Legendre, L.; Rivkin, R.B.; Weinbauer, M.G.; Guidi, L.; Uitz, J. The Microbial Carbon Pump Concept: Potential Biogeochemical Significance in the Globally Changing Ocean. *Prog. Oceanogr.* **2015**, *134*, 432–450. [CrossRef]
11. Tréguer, P.J.; De La Rocha, C.L. The World Ocean Silica Cycle. *Annu. Rev. Mar. Sci.* **2013**, *5*, 477–501. [CrossRef]
12. Kirk, J.T.O. *Light and Photosynthesis in Aquatic Ecosystems*, 3rd ed.; Cambridge University Press: Cambridge, UK; New York, NY, USA, 2011; ISBN 978-0-521-15175-7.
13. Milliman, J.D. Production and Accumulation of Calcium Carbonate in the Ocean: Budget of a Nonsteady State. *Glob. Biogeochem. Cycles* **1993**, *7*, 927–957. [CrossRef]
14. Poulton, A.J.; Adey, T.R.; Balch, W.M.; Holligan, P.M. Relating Coccolithophore Calcification Rates to Phytoplankton Community Dynamics: Regional Differences and Implications for Carbon Export. *Deep. Sea Res. Part II Top. Stud. Oceanogr.* **2007**, *54*, 538–557. [CrossRef]
15. Balch, W.M. The Ecology, Biogeochemistry, and Optical Properties of Coccolithophores. *Annu. Rev. Mar. Sci.* **2018**, *10*, 71–98. [CrossRef]
16. Kondrik, D.V.; Pozdnyakov, D.V.; Johannessen, O.M. Satellite Evidence that *E. huxleyi* Phytoplankton Blooms Weaken Marine Carbon Sinks. *Geophys. Res. Lett.* **2018**, *45*, 846–854. [CrossRef]

17. Kondrik, D.V.; Kazakov, E.E.; Pozdnyakov, D.V.; Johannessen, O.M. Satellite evidence for enhancement of columnal mixing ratio of atmospheric CO_2 over *E. huxleyi* blooms. *Trans. Karelian Res. Cent. Russ. Acad. Sci.* **2019**, *9*, 125–135. [CrossRef]

18. Morozov, E.A.; Kondrik, D.V.; Chepikova, S.S.; Pozdnyakov, D.V. Atmospheric columnar CO_2 enhancement over *E. huxleyi* blooms: Case studies in the North Atlantic and Arctic waters. *Trans. Karelian Res. Cent. Russ. Acad. Sci.* **2019**, *3*, 28–33. [CrossRef]

19. Cermeño, P.; Dutkiewicz, S.; Harris, R.P.; Follows, M.; Schofield, O.; Falkowski, P.G. The Role of Nutricline Depth in Regulating the Ocean Carbon Cycle. *Proc. Natl. Acad. Sci. USA* **2008**, *105*, 20344–20349. [CrossRef]

20. Holligan, P.M.; Fernández, E.; Aiken, J.; Balch, W.M.; Boyd, P.; Burkill, P.H.; Finch, M.; Groom, S.B.; Malin, G.; Muller, K.; et al. A Biogeochemical Study of the Coccolithophore, *Emiliania huxleyi*, in the North Atlantic. *Glob. Biogeochem. Cycles* **1993**, *7*, 879–900. [CrossRef]

21. Young, J. Functions of coccoliths. In *Coccolithophores*; Winter, A., Siesser, W.G., Eds.; Cambridge University Press: Cambridge, UK, 1994; pp. 63–82.

22. Iglesias-Rodríguez, M.D.; Brown, C.W.; Doney, S.C.; Kleypas, J.; Kolber, D.; Kolber, Z.; Hayes, P.K.; Falkowski, P.G. Representing key phytoplankton functional groups in ocean carbon cycle models: Coccolithophorids. *Glob. Biogeochem. Cycles* **2002**, *16*, 47-1–47-20. [CrossRef]

23. Paasche, E. A Review of the Coccolithophorid *Emiliania huxleyi* (Prymnesiophyceae), with Particular Reference to Growth, Coccolith Formation, and Calcification-Photosynthesis Interactions. *Phycologia* **2001**, *40*, 503–529. [CrossRef]

24. Tyrrell, T.; Merico, A. *Emiliania huxleyi*: Bloom Observations and the Conditions That Induce Them. In *Coccolithophores*; Thierstein, H.R., Young, J.R., Eds.; Springer: Berlin/Heidelberg, Germany, 2004; pp. 75–97; ISBN 978-3-642-06016-8.

25. Morozova-Vodyanitskaya, N.V.; Belogorskaya, E.V. On the Significance of Coccolithophores and, Especially, Pontosphere in the Black Sea Plankton. *Tr. Sev. Biol. Stantsii.* **1957**, *9*, 14–21. (In Russian)

26. Pautova, L.A.; Mikaelyan, A.S.; Silkin, V.A. Structure of Plankton Phytocoenoses in the Shelf Waters of the Northeastern Black Sea during the *Emiliania huxleyi* Bloom in 2002–2005. *Oceanology* **2007**, *47*, 377–385. [CrossRef]

27. Mikaelyan, A.S.; Silkin, V.A.; Pautova, L.A. Coccolithophorids in the Black Sea: Their Interannual and Long-Term Changes. *Oceanology* **2011**, *51*, 39–48. [CrossRef]

28. Silkin, V.A.; Pautova, L.A.; Giordano, M.; Chasovnikov, V.K.; Vostokov, S.V.; Podymov, O.I.; Pakhomova, S.V.; Moskalenko, L.V. Drivers of Phytoplankton Blooms in the Northeastern Black Sea. *Mar. Pollut. Bull.* **2019**, *138*, 274–284. [CrossRef]

29. Kopelevich, O.; Burenkov, V.; Sheberstov, S.; Vazyulya, S.; Kravchishina, M.; Pautova, L.; Silkin, V.; Artemiev, V.; Grigoriev, A. Satellite Monitoring of Coccolithophore Blooms in the Black Sea from Ocean Color Data. *Remote Sens. Environ.* **2014**, *146*, 113–123. [CrossRef]

30. Kopelevich, O.V.; Burenkov, V.I.; Vazyulya, S.V.; Sheberstov, S.V. Problems of detection of coccolithophore blooms from satellite data. *Mod. Probl. Remote Sens. Earth Space* **2012**, *9*, 241–250.

31. Churilova, T.; Moncheva, S.; Suslin, V.; Kryvenko, O. Intensity, area extent and frequency of coccolithophores *Emiliania huxleyi* blooms in the Black Sea: Application of remote sensing approach. *Int. Multidiscip. Sci. GeoConference SGEM* **2017**, *17*, 871–879. [CrossRef]

32. Pozdnyakov, D.V.; Pettersson, L.H.; Korosov, A.A. *Exploring the Marine Ecology from Space*; Springer Remote Sensing/Photogrammetry; Springer International Publishing: Cham, Switzerland, 2017; ISBN 978-3-319-30074-0.

33. Pozdnyakov, D.V.; Gnatiuk, N.V.; Davy, R.; Bobylev, L.P. The Phenomenon of *Emiliania huxleyi* in Aspects of Global Climate and the Ecology of the World Ocean. *GES* **2021**, *14*, 50–62. [CrossRef]

34. Cokacar, T.; Kubilay, N.; Oguz, T. Structure of *Emiliania huxleyi* Blooms in the Black Sea Surface Waters as Detected by SeaWIFS Imagery. *Geophys. Res. Lett.* **2001**, *28*, 4607–4610. [CrossRef]

35. Kideys, A.E. Fall and Rise of the Black Sea Ecosystem. *Science* **2002**, *297*, 1482–1484. [CrossRef]

36. Karabashev, G.S.; Sheberstov, S.V.; Yakubenko, V.G. The June maximum of normalized radiance and its relation to the hydrological conditions and coccolithophorid bloom in the Black Sea. *Oceanology* **2006**, *46*, 305–317. [CrossRef]

37. Kopelevich, O.V.; Burenkov, V.I.; Sheberstov, S.V.; Vazulya, S.V.; Sahling, I.V. Coccolithophore Blooms in the North-Eastern Black Sea. In Proceedings of the Twelfth International Conference on the Mediterranean Coastal Environment, Varna, Bulgaria, 6–10 October 2015; MEDCOAST, Mediterranean Coastal Foundation: Dalyan, Turkey, 2015; Volume 1, pp. 363–374.

38. Karabashev, G.S.; Evdoshenko, M.A. Manifestations of the rim current, coccolithophore blooms, and continental runoff in the long-term monthly mean distributions of satellite reflectance coefficients of the Black Sea. *Oceanology* **2015**, *55*, 36–46. [CrossRef]

39. Karabashev, G.S. On the mesoscale structure of the Black Sea satellite images during coccolithophorid bloom. *Remote Sens. Earth Space* **2018**, *15*, 183–190. [CrossRef]

40. Vostokov, S.V.; Vostokova, A.S.; Vazyulya, S.V. Seasonal and Long-Term Variability of Coccolithophores in the Black Sea According to Remote Sensing Data and the Results of Field Investigations. *JMSE* **2022**, *10*, 97. [CrossRef]

41. Sahling, I.V.; Vazyulya, S.V.; Glukhovets, D.I.; Sheberstov, S.V.; Burenkov, V.I.; Yushmanova, A.V. Atlas of Bio-Optical Characteristics of the Russian Seas According to Satellite Ocean Color Scanners. Available online: http://optics.ocean.ru/ (accessed on 18 April 2023).

42. Hedley, J.D.; Mobley, C.D. *Hydrolight 6.0 Ecolight 6.0 Technical Documentation*; Numerical Optics Ltd.: Tiverton, UK, 2019. Available online: https://scholar.google.com/scholar_lookup?title=HYDROLIGHT+6.0+ECOLIGHT+6.0+Technical+Documentation&author=Hedley,+J.D.&author=Mobley,+C.D.&publication_year=2019 (accessed on 18 April 2023).

43. Artemiev, V.A.; Burenkov, V.I.; Vortman, M.I.; Grigoriev, A.V.; Kopelevich, O.V.; Khrapko, A.N. Sea-truth measurements of ocean color: A new floating spectroradiometer and its metrology. *Oceanology* **2000**, *40*, 139–145.

44. Lee, Z.; Carder, K.L.; Mobley, C.D.; Steward, R.G.; Patch, J.S. Hyperspectral Remote Sensing for Shallow Waters. I. A Semianalytical Model. *Appl. Opt.* **1998**, *37*, 6329–6338. [CrossRef]

45. Burenkov, V.I.; Sheberstov, S.V.; Artemiev, V.A.; Taskaev, V.R. Estimation of Measurement Error of the Seawater Beam Attenuation Coefficient in Turbid Water of Arctic Seas. *Light Eng.* **2019**, *27*, 103–111. [CrossRef]

46. Glukhovets, D.I.; Sheberstov, S.V.; Kopelevich, O.V.; Zaytseva, A.F.; Pogosyan, S.I. Measuring the sea water absorption factor using integrating sphere. *Light Eng.* **2018**, *26*, 120–126. [CrossRef]

47. Yushmanova, A.V.; Kopelevich, O.V.; Vazyulya, S.V.; Sahling, I.V. Inter-annual variability of the seawater light absorption in surface layer of the northeastern Black Sea in connection with hydrometeorological factors. *J. Mar. Sci. Eng.* **2019**, *7*, 326. [CrossRef]

48. Holm-Hansen, O.; Riemann, B. Chlorophyll a Determination: Improvements in Methodology. *Oikos* **1978**, *30*, 438–447. [CrossRef]

49. Arar, E.J.; Collins, G.B. *Method 445.0 In Vitro Determination of Chlorophyll a and Pheophytin in Marine and Freshwater Algae by Fluorescence*; United States Environmental Protection Agency: Washington, DC, USA, 1997.

50. Tomas, C.R. *Identifying Marine Phytoplankton*; Academic Press: New York, NY, USA, 1997; p. 858.

51. Throndsen, J.; Hasle, G.R.; Tangen, K.I. *Phytoplankton of Norwegian Coastal Waters*; Almater Forlorlag AS: Oslo, Norway, 2007; ISBN 978-82-7858-037-0.

52. Hillebrand, H.; Dürselen, C.-D.; Kirschtel, D.; Pollingher, U.; Zohary, T. Biovolume Calculation for Pelagic and Benthic Microalgae. *J. Phycol.* **1999**, *35*, 403–424. [CrossRef]

53. Moncheva, S.; Parr, B. Manual for Phytoplankton Sampling and Analysis in the Black Sea. Phytoplankton Manual, UP-GRADE Black Sea Scene Project, FP7. 2010, p. 67. Available online: http://blacksea-commission.org/Downloads/Phytoplankton_%20Mannual-Final-1.pdf (accessed on 3 April 2023).

54. Voss, K.J.; Balch, W.M.; Kilpatrick, K.A. Scattering and Attenuation Properties of *Emiliania huxleyi* Cells and Their Detached Coccoliths. *Limnol. Oceanogr.* **1998**, *43*, 870–876. [CrossRef]

55. NASA's OceanColor Web, Level 1&2 Brouser. Available online: https://oceancolor.gsfc.nasa.gov/cgi/browse.pl (accessed on 18 April 2023).

56. Sheberstov, S.V. A system of batch processing of oceanological satellite data. *Curr. Probl. Remote Sens. Earth Space* **2015**, *12*, 154–161. Available online: http://jr.rse.cosmos.ru/article.aspx?id=1447&lang=eng (accessed on 18 April 2023).

57. Cazzaniga, I.; Zibordi, G.; Mélin, F. Spectral Variations of the Remote Sensing Reflectance during Coccolithophore Blooms in the Western Black Sea. *Remote Sens. Environ.* **2021**, *264*, 112607. [CrossRef]

58. Mobley, C.; Stramski, D.; Bissett, W.; Boss, E. Optical Modeling of Ocean Waters: Is the Case 1–Case 2 Classification Still Useful? *Oceanography* **2004**, *17*, 60–67. [CrossRef]

59. Pope, R.M.; Fry, E.S. Absorption Spectrum (380–700 Nm) of Pure Water II Integrating Cavity Measurements. *Appl. Opt.* **1997**, *36*, 8710–8723. [CrossRef]

60. Röttgers, R.; McKee, D.; Utschig, C. Temperature and Salinity Correction Coefficients for Light Absorption by Water in the Visible to Infrared Spectral Region. *Opt. Express* **2014**, *22*, 25093–25108. [CrossRef]

61. Mobley, C.D. *Light and Water: Radiative Transfer in Natural Waters*; Academic Press: San Diego, CA, USA, 1994; ISBN 978-0-12-502750-2.

62. Loisel, H.; Morel, A. Light Scattering and Chlorophyll Concentration in Case 1 Waters: A Reexamination. *Limnol. Oceanogr.* **1998**, *43*, 847–858. [CrossRef]

63. Morel, A.; Antoine, D.; Gentili, B. Bidirectional Reflectance of Oceanic Waters: Accounting for Raman Emission and Varying Particle Scattering Phase Function. *Appl. Opt.* **2002**, *41*, 6289–6306. [CrossRef]

64. Werdell, P.J.; Franz, B.A.; Bailey, S.W.; Feldman, G.C.; Boss, E.; Brando, V.E.; Dowell, M.; Hirata, T.; Lavender, S.J.; Lee, Z.; et al. Generalized Ocean Color Inversion Model for Retrieving Marine Inherent Optical Properties. *Appl. Opt.* **2013**, *52*, 2019–2037. [CrossRef]

65. Tyrrell, T.; Holligan, P.M.; Mobley, C.D. Optical Impacts of Oceanic Coccolithophore Blooms. *J. Geophys. Res.* **1999**, *104*, 3223–3241. [CrossRef]

66. Kopelevich, O.; Sheberstov, S.; Vazyulya, S. Effect of a Coccolithophore Bloom on the Underwater Light Field and the Albedo of the Water Column. *JMSE* **2020**, *8*, 456. [CrossRef]

67. Kopelevich, O.V.; Sahling, I.V.; Vazyulya, S.V.; Glukhovets, D.I.; Sheberstov, S.V.; Burenkov, V.I.; Karalli, P.G.; Yushmanova, A.V. *Bio-Optical Characteristics of the Seas, Surrounding the Western Part of Russia, from Data of the Satellite Ocean Color Scanners of 1998–2017*; VASh FORMAT, OOO: Moscow, Russia, 2018.

68. Glukhovets, D.; Kopelevich, O.; Yushmanova, A.; Vazyulya, S.; Sheberstov, S.; Karalli, P.; Sahling, I. Evaluation of the CDOM Absorption Coefficient in the Arctic Seas Based on Sentinel-3 OLCI Data. *Remote Sens.* **2020**, *12*, 3210. [CrossRef]

69. Arkhipkin, V.S.; Gippius, F.N.; Koltermann, K.P.; Surkova, G.V. Wind Waves in the Black Sea: Results of a Hindcast Study. *Nat. Hazards Earth Syst. Sci.* **2014**, *14*, 2883–2897. [CrossRef]

70. Mikaelyan, A.S.; Pautova, L.A.; Chasovnikov, V.K.; Mosharov, S.A.; Silkin, V.A. Alternation of Diatoms and Coccolithophores in the North-Eastern Black Sea: A Response to Nutrient Changes. *Hydrobiologia* **2015**, *755*, 89–105. [CrossRef]

71. Drits, A.V.; Nikishina, A.B.; Sergeeva, V.M.; Solov'ev, K.A. Feeding, Respiration, and Excretion of the Black Sea Noctiluca Scintillans MacCartney in Summer. *Oceanology* **2013**, *53*, 442–450. [CrossRef]

72. Burenkov, V.I.; Kopelevich, O.V.; Rat'kova, T.N.; Sheberstov, S.V. Satellite Observations of the Coccolithophorid Bloom in the Barents Sea. *Oceanology* **2011**, *51*, 766–774. [CrossRef]

73. Kubryakov, A.A.; Mikaelyan, A.S.; Stanichny, S.V. Summer and Winter Coccolithophore Blooms in the Black Sea and Their Impact on Production of Dissolved Organic Matter from Bio-Argo Data. *J. Mar. Syst.* **2019**, *199*, 103220. [CrossRef]

74. Kubryakov, A.A.; Mikaelyan, A.S.; Stanichny, S.V. Extremely Strong Coccolithophore Blooms in the Black Sea: The Decisive Role of Winter Vertical Entrainment of Deep Water. *Deep. Sea Res. Part I Oceanogr. Res. Pap.* **2021**, *173*, 103554. [CrossRef]

75. Kubryakova, E.A.; Kubryakov, A.A.; Mikaelyan, A.S. Winter Coccolithophore Blooms in the Black Sea: Interannual Variability and Driving Factors. *J. Mar. Syst.* **2021**, *213*, 103461. [CrossRef]

76. Vostokov, S.V.; Lobkovskiy, L.I.; Vostokova, A.S.; Solov'ev, D.M. Seasonal and Interannual Variability of Phytoplankton in the Black Sea on the Basis of Remote Sensing Data and In Situ Measurements of Chlorophyll-a. *Dokl. Earth Sci.* **2019**, *485*, 293–297. [CrossRef]

77. Vostokova, A.; Vostokov, S.; Saling, I. Regional Features of Seasonal Variability of Phytoplankton in the Black Sea Studied by Remote Sensing Data. In Proceedings of the 28th International Symposium on Atmospheric and Ocean Optics: Atmospheric Physics, Tomsk, Russia, 4–8 July 2022; Romanovskii, O.A., Matvienko, G.G., Eds.; SPIE: Tomsk, Russia, 2022; p. 281. [CrossRef]

78. Gordon, H.R.; Balch, W.M. MODIS Detached Coccolith Concentration Algorithm Theoretical Basis Document, Version 4, Algorithm Theoretical Basis Document. 1999; p. 27. Available online: http://modis.gsfc.nasa.gov/data/atbd/atbd_mod23.pdf (accessed on 3 April 2023).

79. Gordon, H.R.; Boynton, G.C.; Balch, W.M.; Groom, S.B.; Harbour, D.S.; Smyth, T.J. Retrieval of Coccolithophore Calcite Concentration from SeaWiFS Imagery. *Geophys. Res. Lett.* **2001**, *28*, 1587–1590. [CrossRef]

80. Kalinskaya, D.V.; Papkova, A.S. Why Is It Important to Consider Dust Aerosol in the Sevastopol and Black Sea Region during Remote Sensing Tasks? A Case Study. *Remote Sens.* **2022**, *14*, 1890. [CrossRef]

81. Konyukhov, I.V.; Glukhovets, D.I. A set of optical methods for studying marine phytoplankton. *Oceanology* **2017**, *57*, 419–423. [CrossRef]

82. Glukhovets, D.I.; Goldin, Y.A. Express method for chlorophyll concentration assessment. *J. Photochem. Photobiol.* **2021**, *8*, 100083. [CrossRef]